Niki, Y.; Rajasegar, R.; Li, Z.; Musculus, MP.; García-Oliver, JM.; Takasaki, K. (2022). Verification of diesel spray ignition phenomenon in dual-fuel diesel-piloted premixed natural gas engine. International Journal of Engine Research. 23(2):180-197. https://doi.org/10.1177/1468087420983060

Title

Verification of diesel spray ignition phenomenon in dual-fuel premixed natural gas engine

Authors

Yoichi Niki: National Institute of Maritime, Port and Aviation Technology, Tokyo, 181-0004, Japan.

Rajavasanth Rajasegar: Combustion Research Facility, Sandia National Laboratories, Livermore, CA, 94550, USA.

Zheming Li: Combustion Research Facility, Sandia National Laboratories, Livermore, CA, 94550, USA.

Mark P. B. Musculus: Combustion Research Facility, Sandia National Laboratories, Livermore, CA, 94550, USA.

Jose Maria Garcia Oliver: CMT-Motores Térmicos, Universitat Politècnica de València, Spain, Spain.

Koji Takasaki: National institute of maritime, port and aviation technology, Tokyo, 181-0004, Japan.

Corresponding author name and contact details

Yoichi Niki: National Institute of Maritime, Port and Aviation Technology, Tokyo, 181-0004, Japan.

E-mail: niki@m.mpat.go.jp

Abstract

Dual-fuel (DF) engines, in which premixed natural gas and air in an open-type combustion chamber is ignited by diesel-fuel pilot sprays, have been more popular for marine use than pre-chamber spark ignition (PCSI) engines because of their superior durability. However, control of ignition and combustion in DF engines is more difficult than in PCSI engines. In this context, this study focuses on the ignition stability of n-heptane pilot-fuel jets injected into a compressed premixed charge of natural gas and air at low-load conditions. To aid understanding of the experimental data, chemical-kinetics simulations were carried out in a simplified engine-environment that provided insight into the chemical effects of methane (CH_4) on pilot-fuel ignition. The simulations reveal that methane has an effect on both stages of n-heptane autoignition: the small, first-stage, cool-flame-type, low-temperature ignition (LTI) and the larger, second-stage, high-temperature ignition (HTI). As the ratio of pilot-fuel to CH_4 entrained into the spray decreases, the initial oxidization of CH_4 consumes the OH radicals produced by pilot-fuel decomposition during LTI, thereby inhibiting its progression to HTI.

Using imaging diagnostics, the spatial and temporal progression of LTI and HTI in DF combustion are measured in a heavy-duty optical engine, and the imaging data are analyzed to understand the cause of severe fluctuations in ignition timing and combustion completeness at low-load conditions. Images of cool-flame and hydroxyl radical (OH*) chemiluminescence serve as indicators of LTI and HTI respectively. The cycle-to-cycle and spatial variation in ignition extracted from the imaging data are used as key metrics of comparison.

The imaging data indicate that the local concentration of the pilot-fuel and the richness of the surrounding natural-gas air mixture are important for LTI and HTI, but in different ways. In particular, higher injection pressures and shorter injection durations increase the mixing rate, leading to lower

concentrations of pilot-fuel more quickly, which can inhibit HTI even as LTI remains relatively robust. Decreasing the injection pressure from 80 MPa to 40 MPa and increasing the injection duration from 500 microseconds to 760 microseconds maintained constant pilot-fuel mass, while promoting robust transition from LTI to HTI by effectively slowing the mixing rate. This allows enough residence time for the OH radicals, produced by the two-stage ignition chemistry of the pilot-fuel, to accelerate the transition from LTI to HTI before being consumed by CH_4 oxidation.

Thus from a practical perspective, for a premixed natural gas fuel-air equivalence-ratio, it is possible to improve the "stability" of the combustion process by solely manipulating the pilot-fuel injection parameters while maintaining constant mass of injected pilot-fuel. This allows for tailoring mixing trajectories to offset changes in fuel ignition chemistry, so as to promote a robust transition from LTI to HTI by changing the balance between the local concentration of the pilot-fuel and richness of the premixed natural gas and air. This could prove to be a valuable tool for combustion design to improve fuel efficiency or reduce noise or perhaps even reduce heat-transfer losses by locating early combustion away from in-cylinder walls.

Keywords:

dual-fuel engines, lean-premixed natural gas combustion, diesel, two-stage autoignition, cool-flame chemiluminescence, OH* chemiluminescence, ignition delay, chemical kinetics

1. Introduction

Currently, emissions of nitrogen oxides (NOx) and sulfur oxides (SOx) from ocean-going vessels are regulated by the International Maritime Organization (IMO) [1], and natural-gas-fueled marine engines can comply with them without undue additional cost or tradeoffs in engine performance. However, the IMO has a target to reduce greenhouse gas (GHG) emissions from the maritime sector by 50% by 2050 compared to 2008 [2]. By switching the fuel from diesel to natural gas, in principle, 25% of the carbon dioxide (CO_2) emissions from a conventional diesel engine can be cut, as the main component of natural gas is methane (CH_4), which has a 30% lower carbon content by energy than diesel fuel.

Lean-burn natural-gas engines for marine applications can be categorized into two types depending on their ignition/combustion system. One is a pre-chamber spark ignition (PCSI) engine [3] that utilizes a pre-chamber with a spark plug. PCSI systems typically utilize a single fuel, and successful ignition is achieved by means of spark ignition in a typically fuel-rich mixture charged into the pre-chamber, which is situated within the main combustion chamber that contains a more fuel-lean mixture. Ignition and combustion of the lean mixture in the main chamber is promoted by the multiple strong burning-gas jets that emanate from the pre-chamber.

The other type of lean-burn natural-gas engine is a dual-fuel (DF) engine [4], in which a fuel-lean natural-gas mixture in an open-type combustion chamber without a pre-chamber is ignited by diesel-fuel pilot-sprays. DF engines can also be operated as conventional diesel engines, which provides the added advantage of adapting to fuel price fluctuations and in emergency response situations. Though DF engines are more popular than PCSI engines due to the advantages listed earlier, the ignition and combustion process in DF engines is much more complicated due to the nature of

interaction between the natural-gas premixed charge and diesel fuel.

Although in principle natural-gas engines have the potential for lower GHG emissions due to the lower carbon content of the fuel, several recent studies have shown that emissions of unburned CH_4, typically referred to as methane slip, from natural-gas engines can be considerable [5-8]. CH_4 has 84 (cumulative forcing over 20 years) and 28 (cumulative forcing over 100 years) times higher global warming potential relative to CO_2 [9], so even a small amount of methane slip that may be acceptable from an efficiency perspective can have an unacceptable GHG emission penalty. Previous studies indicate that the methane slip primarily comes from unburned mixtures due to crevice mechanisms, such as flame quenching, and misfiring. Crevices that are present inside the combustion chamber act as dead volume that prevent flame propagation and combustion within these volumes [8]. These crevices result in flame quenching close to cylinder walls due to the increased heat loss. Lower combustion pressure and temperature due to leaner natural-gas air mixtures result in increased flame quenching distances [8, 10]. To minimize methane slip, mitigation strategies are that currently being investigated include modification of pilot-fuel injection strategies and combustion control methods [8, 10, 11].

Sometimes a drastic increase in methane slip occurs at low-load conditions in DF engines [6]. This is generally caused by unstable combustion resulting in possible misfire or partial burn, as large cycle-to-cycle variations and increasing tendency to misfire are more pronounced under such low-load conditions. The reason for misfires or partial burns at low-load conditions is most likely due to the unstable ignition characteristics of pilot-fuel sprays and/or unstable flame propagation. Dual-fuel combustion progresses through several overlapping stages: (i) a short transient pilot fuel injection into a premixed natural gas fuel-air mixture, (ii) autoignition of the pilot-fuel and entrained natural gas, (iii) combustion of natural gas in the immediate vicinity of the burning pilot jet and (iv) sequential autoignition and/or premixed turbulent flame propagation of the remaining premixed natural gas. This is further complicated due to multiple degrees of stratification: temperature stratification due to pilot-fuel vaporization-cooling, equivalence-ratio stratification due to partial mixing of the pilot-fuel, and reactivity stratification due to local variations in the ratio of high reactivity pilot-fuel to low reactivity natural gas. Although it is difficult to quantitatively distinguish or isolate the ignition of the pilot-fuel jet from the subsequent ignition and combustion of natural gas, this work primarily focuses on the in-cylinder factors affecting the stability of ignition of pilot-fuel sprays injected into a fuel-lean premixed charge of natural gas and air.

The phenomenology of DF combustion and its underlying processes have been described to some degree in previous optical studies [12,13]. In these studies, an optically accessible rapid-compression-expansion machine (RCEM) equipped with a single-hole coaxial diesel injector is utilized to investigate the DF combustion, as it transitions from ignition to premixed-flame combustion using thermodynamic analysis as well as OH* chemiluminescence imaging and planar laser-induced fluorescence (PLIF) imaging of CH_2O. The optical diagnostics showed that CH_4 increases the ignition delay and prolongs the pilot-fuel combustion duration. This effect is amplified for pilot-fuel injection strategies that lead to leaner pilot-fuel mixtures at ignition. Other RCEM studies also show that the CH_4 in the natural-gas premixed charge that is entrained into the pilot-fuel spray before ignition

prolongs the ignition delay of the pilot-fuel due to its chemical-inhibition effects [14,15].

In addition to studies on the chemical effects of CH_4 on pilot-fuel ignition and combustion, other studies have focused on the influence of pilot-fuel injection parameters including injection pressure and injection duration on DF combustion [16-19]. Previous studies on DF combustion have reported a tradeoff between low unburned hydrocarbon (UHC) emissions and low NO_x and soot emissions. Increased pilot-fuel mass results in more complete combustion of the premixed natural gas charge, but soot and NO_x emissions tend to increase [19, 20]. Conversely, with lower pilot-fuel mass, combustion performance tends to deteriorate due to the high sensitivity of ignition delay to changes in premixed natural gas concentration [20], which leads to large cycle-to-cycle variations and increasing tendency to misfire. In many applications, maximizing the replacement of diesel fuel by natural gas, with energy ratios as high as 95% (80% in this study) is of interest. Also to minimize NOx emissions, the pilot-fuel quantity is usually kept as low as possible in heavy-duty DF engines. NOx emissions generally tend to increase with the increase in pilot-fuel quantity and injection pressure [15, 16, 19]. These studies have also shown that the autoignition of the pilot fuel is strongly affected by the concentration of CH_4 in the natural-gas premixed charge [16, 17], and that the pilot-fuel injection pressure is an important parameter affecting flame propagation in DF combustion [18, 19, 21]. A reduction of the fuel-rail pressure appears to be effective in altering the diesel-pilot ignition characteristics. Lower injection pressures lead to higher pilot-fuel concentrations within the sprays and therefore increase the ignition probability [18, 19, 21].

Although the above-mentioned studies provide valuable insight into the in-cylinder processes of DF engines when the ignition and combustion processes are stable, comparatively little is known about unstable ignition and combustion with frequent misfiring that can result in excessive methane slip. This work intends to further investigate the underlying physics of unstable ignition of the pilot-fuel spray in the presence of premixed natural-gas. To complement the experimental data, chemical-kinetics simulations in a simplified engine-environment are carried out to provide additional understanding of the chemical effects of CH_4 on the pilot-fuel ignition characteristics. The simulations reveal that CH_4 has an effect on both stages of n-heptane autoignition: the small, first-stage, cool-flame-type, low-temperature ignition (LTI) and the larger, second-stage, high-temperature ignition (HTI). Using imaging diagnostics, the spatial and temporal progression of LTI and HTI in DF combustion are measured in a heavy-duty optical engine, and these imaging data are analyzed to understand the cause of severe fluctuations in ignition timing and combustion completeness at low-load conditions. In these experiments, eight fuel-sprays of n-heptane pilot-fuel are injected from the center of the combustion chamber into a compressed premixed charge of natural gas and air at low-load conditions. The diagnostics capture images of cool-flame and hydroxyl radical (OH*) chemiluminescence that serve as indicators of LTI and HTI respectively. The cycle-to-cycle and spatial variation in ignition extracted from the imaging data are used as key metrics of comparison.

Based on the insight gained from the experimental measurements and simulations, possible solutions involving the manipulation of pilot-fuel injection parameters are identified, which has the potential to minimize ignition fluctuations, avoid misfires or partial burns and minimize methane slip. From a practical perspective, for a given target equivalence ratio of the premixed natural-gas and air,

the pilot-injection parameters can be suitably manipulated to promote a robust transition from LTI to HTI. Accordingly, the balance between the local concentrations of the pilot-fuel and the equivalence ratio of the surrounding natural-gas air mixture is analyzed for both experiments and simulations with the practical aim of determining key pilot-fuel injection parameters that can be modified to improve the ignition characteristics of pilot-fuel injections into natural-gas and air mixtures. Further investigations on optimization of the pilot-fuel injection parameters that suits each operating equivalence ratio will be pursued in the future.

2. Chemical-kinetics simulations and Experimental setup

2.1 Chemical-kinetics simulations

The chemical kinetics of n-heptane combustion in the presence of CH_4 is simulated to understand the chemical inhibition effect of natural gas on pilot-fuel autoignition characteristics. These simulations are not intended to predict all of the in-cylinder processes, but rather to isolate the chemical effects of variations of the premixed natural-gas concentration on the ignition delay in a series of canonical scenarios to aid interpretation of experimental data.

While higher-fidelity combustion models that capture both fluid-mechanic and chemical processes could be used in conjunction with an experiment like the one described here, the simple homogeneous closed reactor model decouples chemistry from the other simultaneous, complex, thermo-fluidic processes, leading to a more straightforward parametric understanding of in-cylinder effects. The simulations use a zero-dimensional, closed homogeneous reactor [22] to model n-heptane ignition under constant-pressure conditions. The simulations are performed in Cantera [23] using the Lawrence Livermore National Laboratory detailed n-heptane mechanism version 3.1 [24], which also includes chemistry for methane, ethane, and propane of the synthetic natural gas.

2.2 Optical engine and imaging setups

A single cylinder heavy-duty optical engine, whose schematic layout is shown in Fig. 1, is used in this study under operating conditions representative of a practical dual-fuel engine. As shown in Table 1, the engine has a 13.97 cm bore and a displacement of 2.34 L. It is equipped with a Bowditch optical piston with an open, right-cylindrical bowl and a flat, fused-silica, piston-crown window to allow imaging access to the bowl, when viewed from below. Further details about this engine can be found in our previous work [25]. In this study, the engine has been modified and fitted with a natural-gas fueling system as described below.

2.3 Natural-gas fumigation and pilot-fuel injection systems

The specifications of the natural-gas fumigation injector and the pilot-fuel injector are shown in Table 1. A Clean Air SP010, solenoid-actuated, single-hole gas injector fitted in the intake manifold, 0.55 m upstream of the intake port fumigates natural gas into the intake air stream using a perforated ring embedded in the intake flow. The natural gas is a surrogate mixture of 95% methane, 4% ethane, and 1% propane by volume.

A Delphi DFI 1.5 light-duty, solenoid-actuated, common-rail injector with eight equally spaced 0.131-mm orifices is used for its fast response time and its ability to deliver consistent, short-duration pilot injections. The pilot-fuel is high-purity n-heptane with ignition properties similar

to that of diesel fuel [26].

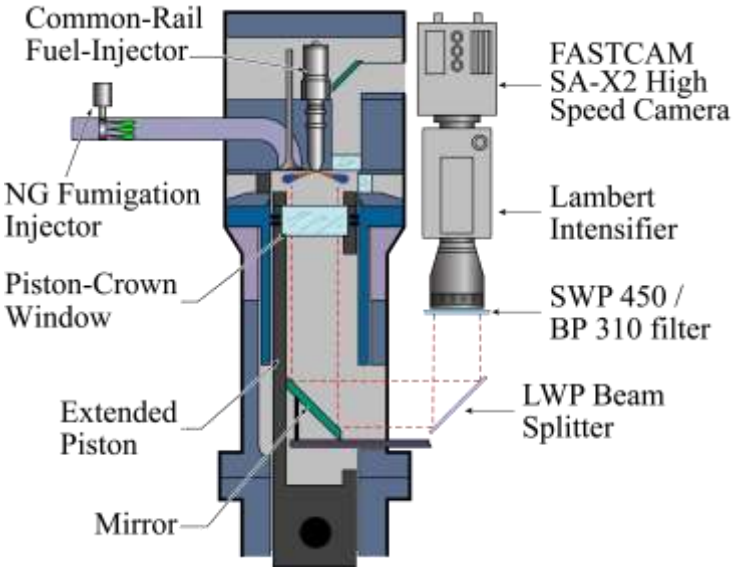

Figure 1. Schematic layout of the optical engine with imaging diagnostics setup.

Table 1. Engine and injector specifications.

Engine Specifications	
Engine base type	Cummins N-14, DI diesel
Bore x Stroke [cm]	13.97 x 15.24
Displacement [liters]	2.34
Compression Ratio	11.2
Combustion Chamber	Quiescent, direct injection
Bowl Width, Depth [cm]	9.78, 1.55
Swirl ratio	0.5
Natural Gas Fumigation Injector Specifications	
Fuel injector type	Solenoid actuated, Clean Air SP010 Gas Injector
Number of holes	1
Fuel gas	Surrogate natural gas (95% CH_4, 4% C_2H_6 1% C_3H_8 by vol.)
Pilot Fuel Injector Specifications	
Fuel injector type	Common Rail, solenoid-actuated Delphi DFI 1.5
Orifices and diameter [mm]	8 equally-spaced, 0.131
Included spray angle	156º
Fuel	n-heptane

2.4 Cylinder Pressure and Optical Diagnostics

Several key diagnostics measure the spatial and temporal autoignition characteristics of n-heptane injections into premixed natural gas, including cylinder-pressure measurements and optical imaging. Cylinder pressure is measured with an AVL QC34D piezoelectric pressure transducer and

recorded every quarter crank angle degree (ºCA). The apparent heat-release rate (AHRR) calculations are based on thermodynamic analysis of the cylinder pressure [27]. Air is treated as an ideal gas for the working fluid, heat losses are ignored, and the specific-heat ratio is calculated based on the thermochemical properties of the mixture by using Cantera [23].

Insight into the spatial and temporal autoignition characteristics of the transient n-heptane jets injected into premixed natural gas is provided by two different chemiluminescence imaging techniques: Crank-angle resolved, non-simultaneous, first-stage, cool-flame (broadband-blue) chemiluminescence [28], and second-stage, high-temperature filtered OH* chemiluminescence [29]. Chemiluminescence images are captured by a Photron FASTCAM SA-X2 high-speed camera coupled to a Lambert Hi-CATT high-speed intensifier with an S-20 photocathode. The exposure time and resolution of the high-speed camera are set to 50 microseconds and 768 x 768 pixels respectively. The high-speed images are captured every 0.5 ºCA. The gate width and the gain of the intensifier are set 50 microseconds and 80% respectively.

The first-stage, cool-flame chemiluminescence images are captured during LTI using a 105 mm glass (visible) Nikkor lens at a fully open aperture (f/2.5) setting fitted with a 415-440 nm band-pass filter (BPF). This combination of glass lens and BPF rejects chemiluminescence from the ultra-violet (UV) range (i.e., OH* chemiluminescence near 310 nm does not contribute to the cool-flame images presented). Furthermore, the filter also rejects long-wavelength (green through IR) soot luminosity, though soot luminosity is unlikely to be present during LTI. Hence, the recorded LTI luminosity is most likely dominated by chemiluminescence from HCHO*, HCO*, CH*, CO_2*, and/or broadband emission from the CO continuum [30, 31]

The second-stage, HTI, as indicated by OH* chemiluminescence, is imaged using a 105-mm UV Nikkor lens with the aperture set between f/4.5 and f/22 depending on experimental conditions to avoid saturation, in conjunction with a 310-nm BPF with a 10-nm full width at half-maximum. Excited-state hydroxyl radical OH* is produced during HTI and provides an indication of both HTI and subsequent flame-propagation/distributed-ignition combustion that follows.

2.5 Engine operating condition and test matrix

The engine is operated at fixed speed of 1200 min^{-1} for all experiments. The engine is motored by a dynamometer until the engine speed and intake pressure stabilize, after which the measurement sequence is initiated. The engine is operated in a “skip-fire” mode, where every fired cycle (i.e., with a pilot injection) is followed by nine consecutive motored cycles (no pilot injections). The 9:1 skip-fire strategy is adopted in the optical engine mainly as a safeguard against large thermal gradients that can cause severe damage to the optical windows. This strategy also allows for a fundamental study of the governing processes, as there is sufficient time for continuous gas-exchange to take place, which removes any residuals from the previous fired cycle and thus eliminates its impact on combustion in the subsequent fired cycles. This sequence is then repeated 30 times for each engine run. The pilot-fuel injector solenoid energization-timing is held constant at 13 crank angle degrees (CAD) before top dead center (TDC). The natural-gas fumigation injections are initiated five cycles before the firing cycle to ensure a relatively homogenous premixed charge at the end of the compression stroke. Though not described in this manuscript, infrared (IR) imaging [21] was carried out to quantify in-cylinder

natural gas concentration and to characterize the n-heptane pilot-fuel jet under non-reactive conditions using nitrogen ambient. The IR images confirmed the presence of a homogenous premixed charge in the combustion chamber.

As specified in Table 2, three different pilot-fuel injection parameter combinations of fuel-rail pressure P_{inj} (injection pressure) and solenoid energization-duration t_{SE} (injection duration) are investigated: (1) 80 MPa and 500 microseconds, (2) 80 MPa and 760 microseconds, and (3) 40 MPa and 760 microseconds. These combinations are selected so that the data could be compared on the basis of identical injection-pressure using (1) and (2), identical injection-duration using (2) and (3), and equal pilot-fuel mass using (1) and (3). The pilot-fuel mass injected is determined by collecting and weighing the injected fuel over a total of 100 injections for the three different pilot-fuel injection parameter combinations used in this study. The combined "signal and hydraulic delay" for the commanded injection start and injection end is estimated to be consistently around 2.5 CAD and 3.5 CAD respectively based on IR imaging (not shown here) [21, 32].

The above-mentioned three pilot injections are tested under two intake pressure conditions of P_{IN} = 0.1 and 0.2 MPa while the intake air temperature T_{IN} was maintained constant at 100°C (within +/-3°C). These intake pressures correspond to low-load and mid-load operating conditions of a typical DF engine. As the intake pressure is increased from 0.1 MPa to 0.2 MPa, the corresponding cylinder pressure increases from about 2 MPa to 4.5 MPa at the start of injection resulting in higher charge density. Based on IR imaging, at P_{IN} = 0.2 MPa, the pilot-fuel jet exhibited a slower rate of penetration (roughly 25% slower) due to the increased charge density (~2.25 times higher). This might possibly result in a reduced entrainment on a volume basis. However, the mass entrained is still higher due to the increased charge density leading to rapid vaporization of the pilot-fuel jet resulting in a shorter ignition delay. As discussed earlier, since the overall objective of this study is to understand the underlying physics leading to unstable ignition of the pilot-fuel injections in the presence of a premixed natural-gas air charge under low-load conditions, the results for P_{IN} = 0.1 MPa will be discussed at length in this work.

For each combination of pilot-fuel injection parameters and intake pressure, the premixed natural-gas concentration is varied from a pre-pilot natural-gas equivalence ratio (ϕ_{NG}) of zero (pure n-heptane only, diesel-only operation) to ϕ_{NG} = 0.5 (typical of marine DF engines), in steps of 0.1. This sweep allowed for a fundamental study focused on isolating the inhibition effect of natural gas on pilot-fuel autoignition. From a practical perspective, ϕ_{NG} = 0.5 is interesting for low NOx, high efficiency, and manageable peak heat release. The short pilot-fuel injections allow to maximize diesel-fuel replacement by natural gas while maintaining sufficiently low COV in IMEP across the range of conditions tested, even if the unburned natural gas emissions might be greater than for a more optimized condition. Since the mass of natural gas that exists before the pilot injection varies with ϕ_{NG}, the fraction of total fuel lower-heating-value (LHV) from the piloted n-heptane also varies for each condition as listed in Table 3.

Table 2. Experimental conditions.

Simulated load	Pilot injection condition no.	Pilot fuel mass	Pilot injection pressure (fuel-rail pressure) P_{inj}	Pilot injection duration (solenoid energization duration) t_{SE}	Intake air pressure P_{IN}	Intake air temperature T_{IN}	Pre-pilot natural gas equivalence ratio ϕ_{NG}
		[mg]	[MPa]	[micro seconds]	[MPa]	[ºC]	[-]
Low	(1)	11.5	80	500	0.1	100	0, 0.1, 0.2, 0.3, 0.4, 0.5
Low	(2)	24.3	80	760			
Low	(3)	11.5	40	760			
Mid	(1)	11.5	80	500	0.2		
Mid	(2)	24.3	80	760			
Mid	(3)	11.5	40	760			

Table 3. Fraction of total fuel LHV (%) from n-heptane as pilot fuel.

Simulated load	Pilot injection condition no.	Fraction of total LHV from n-heptane					
		ϕ_{NG} = 0.0	0.1	0.2	0.3	0.4	0.5
		[%]					
Low	(1)	100	41	26	19	15	13
Low	(2)	100	59	42	33	27	23
Low	(3)	100	41	26	19	15	13
Mid	(1)	100	26	15	10	8	7
Mid	(2)	100	42	27	20	16	13
Mid	(3)	100	26	15	10	8	7

3. Chemical-kinetics simulations results and discussion

Constant pressure combustion simulation results from autoignition of gas-phase n-heptane under stoichiometric conditions at an initial temperature of 800 K (estimated adiabatic temperature accounting for fuel vaporization-cooling) and two initial pressures of 2 MPa ($\boldsymbol{P_{IN}}$ = 0.1 MPa) and 4.5 MPa ($\boldsymbol{P_{IN}}$ = 0.2 MPa) for varying CH_4 concentrations are shown in Fig. 2(a) and 2(b) respectively. The initial temperature and pressures corrrespond to the thermodynamics conditions inside the combustion chamber at the start of pilot-fuel injection (10.5 CAD before TDC) for the two intake pressure conditions. Though a range of mixture compositions may exist within the pilot-fuel jet, the stoichiometric mixture used in these simulations is representative and consistent with the definition of a “most-reactive mixture fraction” [33]. Furthermore, the simulations are not intended to cover the entire range of mixture compositions (and temperature) that exists in the engine during the mixing process of the pilot-fuel with the premixed charge but rather to provide a representative case that

elucidates the inhibition effect of natural gas on n-heptane autoignition. At near TDC conditions, the change in cylinder pressure is minimal (refer to Fig.7) so the constant pressure assumption for combustion simulation is fairly reasonable at least during the initial phase of combustion, i.e., the first-stage, LTI and its transition into second-stage, HTI, which is the main focus of this work. It is to be noted that the isobaric combustion assumption may not be valid during the later stages of combustion that results in increasing cylinder pressure due to significant heat release.

Figure 2(a) and 2(b) show the time-resolved evolution histories of temperature and key species including n-heptane (C_7H_{16}), CH_4, OH, CH_2O, and ketohydroperoxide (KHP) for 0%, 3% and 5% volume addition of CH_4 to n-heptane/air mixtures at $\boldsymbol{P_{IN}}$ = 0.1 MPa and $\boldsymbol{P_{IN}}$ = 0.2 MPa respectively. CH_4 is added in varying concentrations to the existing stoichiometric mixture of n-heptane and air while the mass of n-heptane is kept constant. These varying CH_4 concentrations correspond to pre-pilot natural-gas equivalence ratio $\boldsymbol{\phi_{NG}}$ = 0.0, 0.3, and 0.5, respectively. The inhibition effect of CH_4 on n-heptane autoignition is likely due to the combination of reduced oxygen concentration, increased mixture thermal capacity, and CH_4 acting as a radical sink. Due to 5% volume addition of CH_4 to a stoichiometric mixture of n-heptane and air, the O_2 concentration changes by only 1% (drops to 19.6% from 20.6%). Thus, since the reduction in oxygen intake partial pressure [34] due to the displacement of air by natural gas is minimal, the simulation results are primarily discussed in terms of the chemical inhibition effect of CH_4 on pilot-fuel autoignition rather than solely due to its thermo-physical properties, such as the heat capacity ratio effect.

Irrespective of CH_4 concentration, the temperature histories do exhibit the characteristic two-stage autoignition behavior, i.e., a small temperature rise (~200 K) due to LTI, followed by a delay (dwell) period and a subsequent increase in temperature exceeding 2000 K due to the HTI and ensuing combustion. However, at higher intake pressure, the dwell period following LTI is much shorter as shown in Fig. 2(b).

The essential role played by the key intermediate species (shown in Fig.2) in the autoignition process of n-heptane has been well documented in the literature [35]. KHP tends to accumulate during the initial phase of LTI reactions. Then, following a small temperature rise as LTI reactions continue to proceed further, KHP rapidly decomposes forming OH and CH_2O. Highly reactive OH radicals further attack n-heptane and CH_4 leading to their continued decomposition as highlighted in Fig. 2, resulting in the progress of subsequent chain-branching reactions after LTI. Decomposition of CH_2O eventually produces H_2O_2, which continues to dissociate, generating more OH during the second-stage, HTI reactions. Thus, the combined OH production due to KHP and H_2O_2 decomposition exceeding OH consumption due to fuel oxidation, signifies the onset of second-stage HTI reactions leading to the main heat-release. From Fig. 2, it is clear that the onset of KHP decomposition is delayed by the presence of increasing concentrations of CH_4. Moreover, the presence of CH_4 also prolongs the dwell time (thermal ignition preparation time) between LTI and HTI [36].

The bottom panel of Fig. 3 shows the OH formation and destruction rates for 5% CH_4 addition ($\boldsymbol{\phi_{NG}}$ = 0.5) to a stoichiometric mixture of n-heptane and air. Since the initial production and destruction rates of OH are fairly similar, only a small increase in OH concentration is observable after 2 milliseconds as shown in Fig. 2(a). The complete reaction pathway outlining the formation and

destruction of OH radical in the combustion of a long-chain hydrocarbon such as n-heptane is complex and beyond the scope of this work. However, the following reactions were identified to be the most dominant reactions responsible for OH destruction based on their reaction rates. Moreover, these particular set of reactions were chosen as they can adequately portray the complex interplay and balance that exists in destruction of OH due to the competing effects of chain initiation reactions (n-heptane, H-abstraction: R1-R4), OH capture by natural gas (inhibitive effect: R5) and CH_2O oxidation (R6) resulting in heat release.

$nC_7H_{16} + OH <=> C_7H_{15}$ (H abstraction from C1) $+ H_2O$ (R1)

$nC_7H_{16} + OH <=> C_7H_{15}$ (H abstraction from C2) $+ H_2O$ (R2)

$nC_7H_{16} + OH <=> C_7H_{15}$ (H abstraction from C3) $+ H_2O$ (R3)

$nC_7H_{16} + OH <=> C_7H_{15}$ (H abstraction from C4) $+ H_2O$ (R4)

$CH_4 + OH <=> CH_3 + H_2O$ (R5)

$CH_2O + OH <=> H_2O + HCO$ (R6)

The top panel of Fig.3 shows the individual contribution ratio to OH destruction for reactions R1 through R6 for the 5% CH_4 addition ($\phi_{NG} = 0.5$) case presented in Fig.2. The contribution ratio to OH destruction is defined as the reaction rate of each individual reaction divided by the total OH destruction rate. The C_7H_{16} reaction is the summation of reactions R1 through R4. The consumption of OH due to CH_4 decomposition (contribution ratio) is consistently at 10% or higher until around 2.0 milliseconds, which marks the onset of HTI. The consumption of OH by CH_4 (reaction R5) hinders reactions that lead to C_7H_{16} decomposition (chain initiation reactions R1-R4) and CH_2O oxidation by OH (reaction R6). In particular, reaction R6 plays a significant role in the H_2O_2 reaction loop which dominates the heat release during dwell time [36]. The H_2O_2 reaction loop results in gradual heat release until sufficient temperature is attained for HTI. CH_4 can also compete with C_7H_{16} in reacting with other highly reactive intermediates such as H and O. These competing effects delay the decomposition of C_7H_{16} (reactions R1-R4), CH_2O oxidation by OH (reaction R6) and restrict the availability of other highly reactive intermediates, as they get consumed through CH_4 decomposition, which results in prolonging the onset of first-stage, LTI and second-stage, HTI. Thus, the chemical kinetics simulations reveal that the characteristic two-stage autoignition behavior of n-heptane is strongly influenced by the presence of CH_4, which increasingly delays the onset of both LTI and HTI reactions and the dwell time between them with increasing CH_4 concentrations.

The optical imaging studies described in the following sections will be used to successfully complement and validate the valuable insights gained from the chemical kinetics simulations. In this context, cool-flame (broadband) and OH* chemiluminescence are employed to detect the onset of LTI and HTI reactions, thereby to analyze the associated spatial and temporal variability to characterize the ignition of n-heptane pilot-fuel jets in the presence of natural gas.

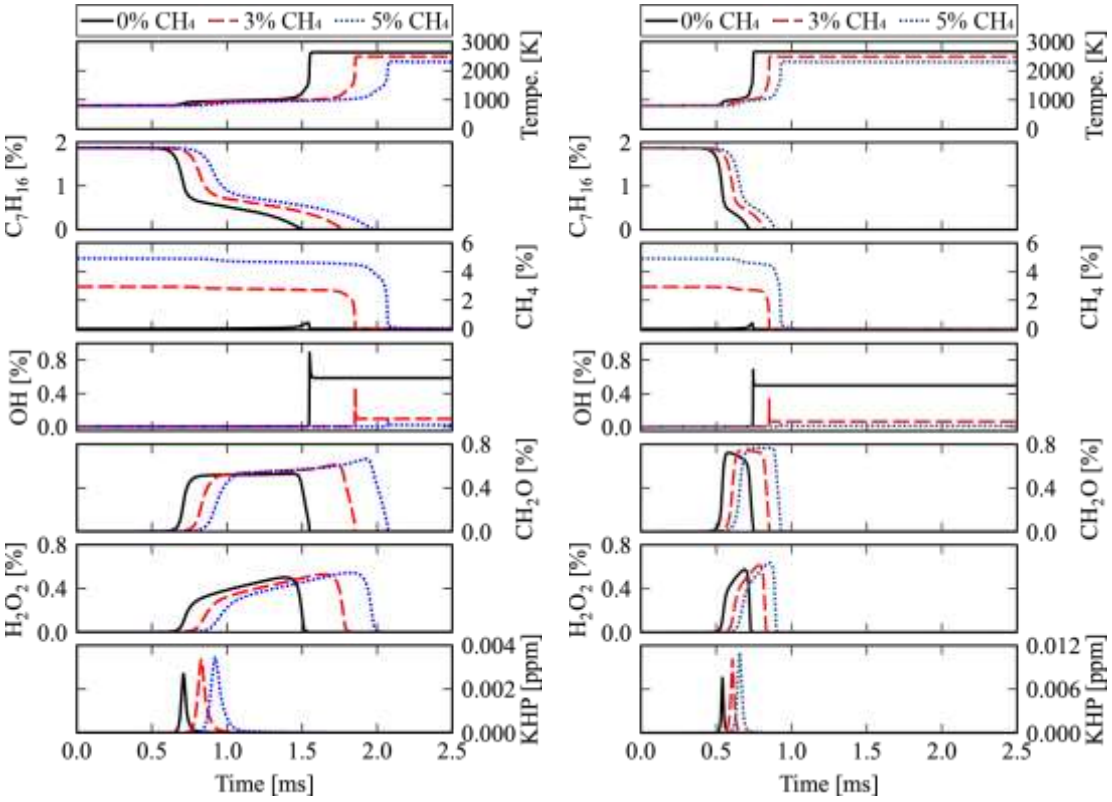

(a) Initial condition: 800 K and 2 MPa (low-load condition: P_{IN} = 0.1 MPa)

(b) Initial condition: 800 K and 4.5 MPa (mid-load : P_{IN} = 0.2 MPa)

Figure 2. Time evolution of temperature and key intermediate species based on chemical-kinetics simulations of stoichiometric n-heptane vapor ignition at initial conditions of (a) 800 K and 2 MPa (low-load condition: P_{IN} = 0.1 MPa) and (b) 800 K and 4.5 MPa (mid-load : P_{IN} = 0.2 MPa) for varying CH_4 concentrations.

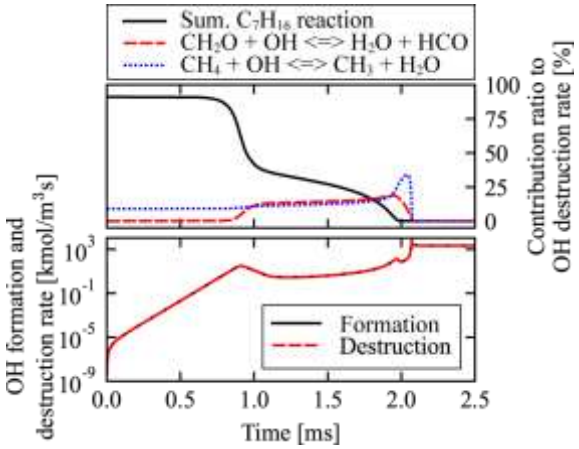

Figure 3. OH species formation and destruction rates for most dominant reactions along with their individual contribution ratio to OH destruction for 5% CH_4 concentration.

4. Experimental results and discussion

4.1 LTI and HTI detection based on optical imaging diagnostics

Representative snapshots captured at key crank angle timings from two different cycles (non-sequential) using the two previously described optical setups for cool-flame chemiluminescence

during LTI and OH* chemiluminescence from HTI are shown in Figs. 4 and 5 respectively. Below these sets of chemiluminescence images are plots of temporal evolution of the mean image intensity, i.e., spatially averaged image-intensity over the entire piston-bowl. The timings corresponding to instances when the snapshots were captured are indicated by means of vertical lines in the intensity plots.

To aid comparison and to highlight the influence of natural gas on the pilot-fuel ignition characteristics, chemiluminescence images from n-heptane pilot-fuel injections into two different ambient compositions are shown in Figs. 4 and 5 along with their corresponding cylinder pressure and AHRR profiles: (a) ambient is air without natural gas ($\phi_{NG} = 0.0$), and (b) ambient is a premixed charge of natural gas and air ($\phi_{NG} = 0.5$).

In all cases, the AHRR profile exhibits a typical two-stage heat release feature, i.e., a small, first-stage heat-release (LTI) preceeding the main, second-stage heat-release (HTI). Figure 4 clearly shows that the temporal evolution of the mean cool-flame chemiluminescence intensity closely follows the corresponding AHRR profiles until the onset of HTI, i.e., the start timing of the LTI and HTI from the AHRR correlates well with the mean intensity profiles.

Comparing cases (a) and (b) in Fig. 4, it is clear that the presence of natural gas delays the start of LTI and prolongs the dwell time between LTI and HTI. These experimental findings are in line with the results of chemical-kinetics simulations described earlier in Section 3. Despite the saturation observed in the cool-flame chemiluminescence images near the start of HTI at 362 CAD in case (a) and at 372 CAD in case (b), the spatial and temporal evolution of cool-flame chemiluminescence remains gradual (increasing and then decreasing resulting in a small bump) during the course of first-stage heat release (LTI), i.e, between 358 to 361 CAD in case (a) and between 362 to 364 CAD in case (b). Also, since the OH* chemiluminescence images shown in Fig. 5 primarily represent the evolution of HTI and the subsequent combustion process, the corresponding mean intensity profiles do not reflect the LTI represented by the small bump in the associated AHRR. However, the mean intensity profile of OH* chemiluminescence imaging does resemble the second-stage AHRR both in terms of timing and duration.

Comparing the temporal evolution of mean intensity of cool-flame and OH* chemiluminescence presented in Figs. 4 and 5 respectively, it is clear that the timing of the sharp increase in cool-flame chemiluminescence intensity after LTI (as seen in Fig. 4) is consistent with the start timing of the rising OH* chemiluminescence intensity (as seen in Fig. 5). Figure 6 outlines the methodology used in the detection of the start and end of LTI and the start of HTI, with the time elapsed between the end of LTI and the start of HTI defined as the associated dwell time. The start and end of LTI are defined based on the local maxima of the second time-derivative of the mean intensity of cool-flame chemiluminescence imaging. The start of HTI is defined as the time after the end of LTI when the first time-derivative of the mean intensity of cool-flame chemiluminescence imaging exceeds 20% of its peak value.

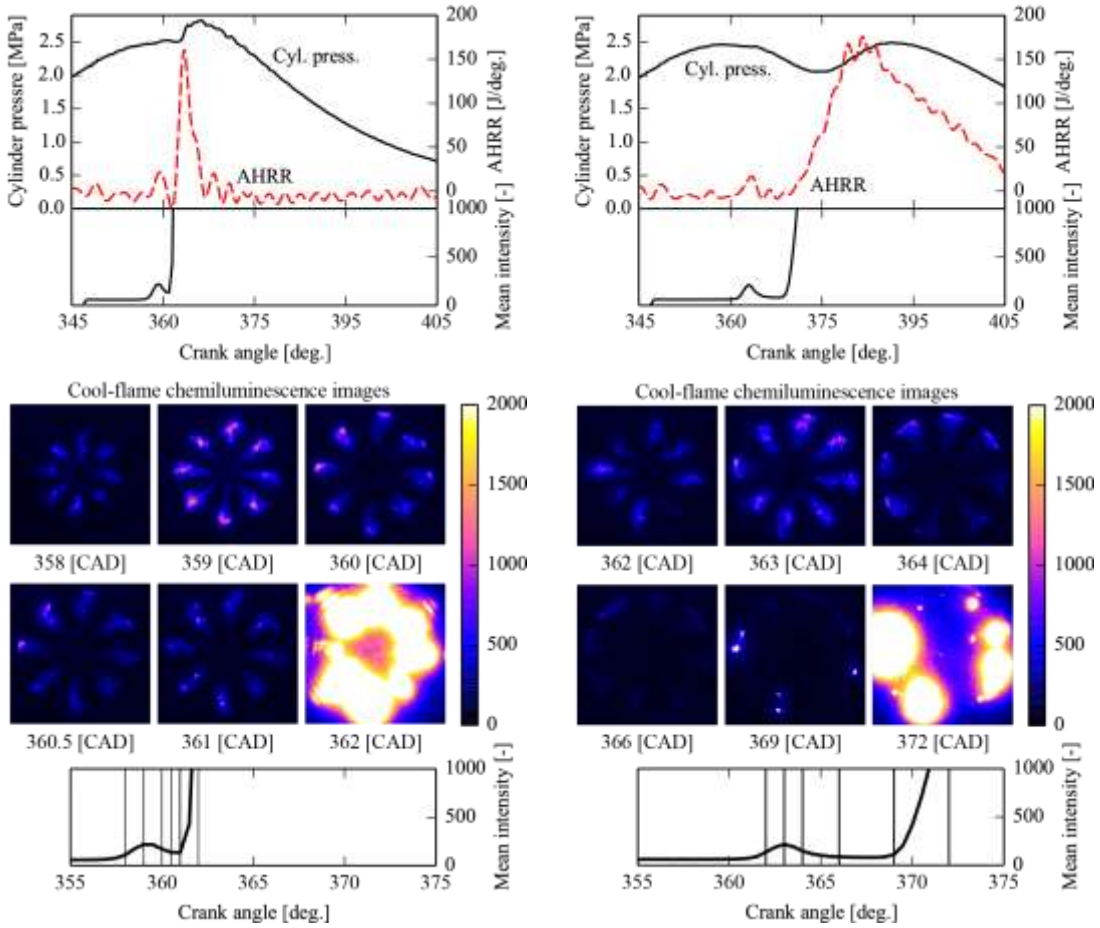

(a) ϕ_{NG} = 0.0 (b) ϕ_{NG} = 0.5

Figure 4. Top: Cylinder pressure, AHRR, and spatially-averaged cool-flame chemiluminescence intensity. Bottom: Snapshots of representative cool-flame chemiluminescence images taken at key crank angle timings (during LTI) indicated by the labels and the vertical lines in mean intensity profile plots. (a) Ambient is air without natural gas (ϕ_{NG} = 0.0); (b) Ambient is a premixed charge of natural gas and air (ϕ_{NG} = 0.5). Pilot fuel-injection condition (3): t_{SE} = 760 microseconds, P_{inj} = 40 MPa; P_{IN} = 0.1 MPa. Data presented are from a single individual cycle that is considered representative of the entire dataset.

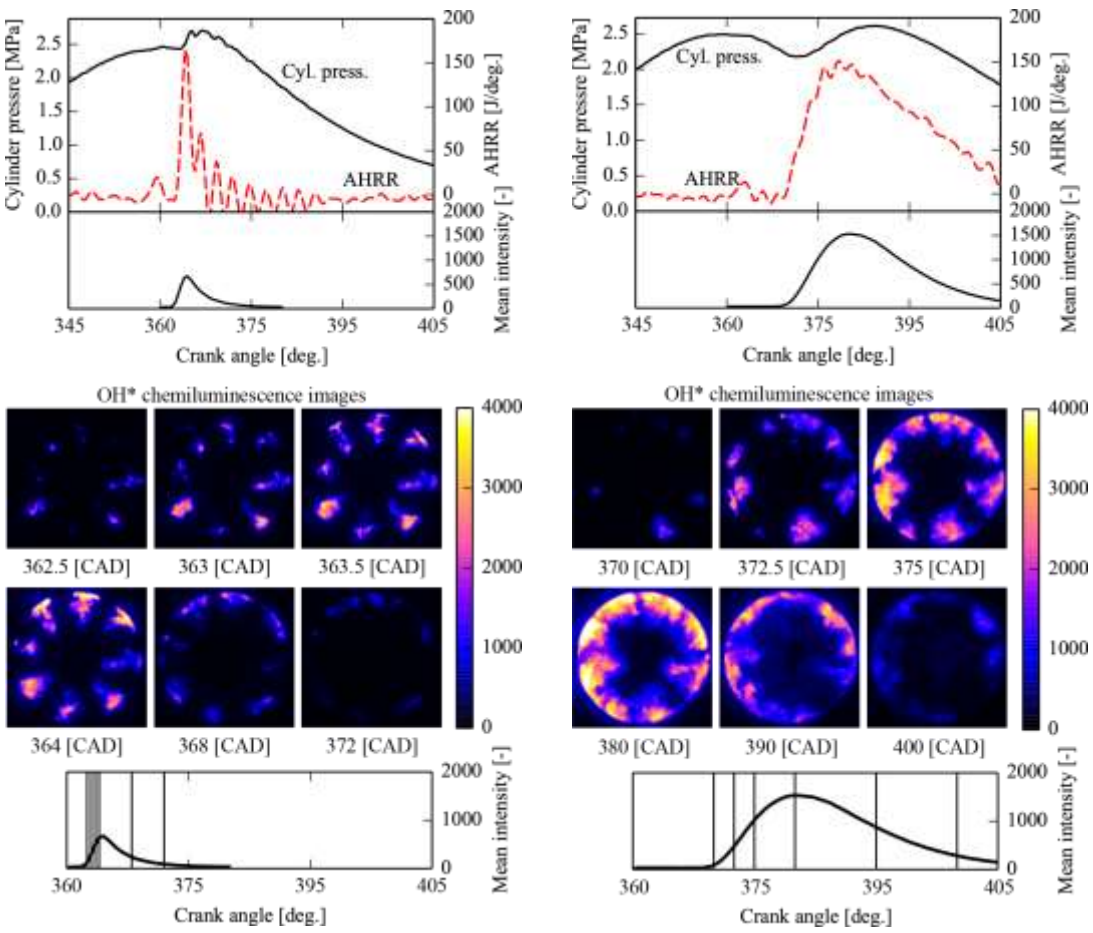

(a) ϕ_{NG} = 0.0 (b) ϕ_{NG} = 0.5

Figure 5. Top: Cylinder pressure, AHRR, and spatially-averaged OH* chemiluminescence intensity. Bottom: Snapshots of representative OH* chemiluminescence images taken at key crank angle timings (during HTI) indicated by the labels and the vertical lines in mean intensity profile plots. (a) Ambient is air without natural gas (ϕ_{NG} = 0.0); (b) Ambient is a premixed charge of natural gas and air (ϕ_{NG} = 0.5). Pilot fuel-injection condition (3): t_{SE} = 760 microseconds, P_{inj} = 40 MPa; P_{IN} = 0.1 MPa. Data presented are from a single individual cycle that is considered representative of the entire dataset.

1

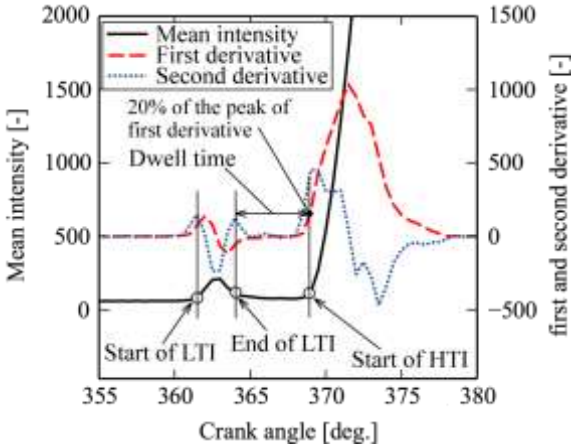

Figure 6. A typical spatially-averaged cool-flame chemiluminescence intensity profile indicating

the definitions for start and end of LTI, start of HTI, and the associated dwell time.

4.2 Combustion Stability Analysis

From the 30 fired cycles that constitute each engine run, only the last 16 consecutive fired cycles are selected for analysis to minimize any variation caused due to the gradual warm up of the engine or transients in the natural gas supply pressure and pilot-fuel injection pressure. Furthermore, analysis of cylinder pressure data from the 16 fired cycles indicate fairly constant thermodynamic conditions at start of injection. The maximum variation (standard deviation) in measured cylinder pressure at the start of injection is 31 kPa for P_{IN} = 0.1 MPa and 57.2 kPa P_{IN} = 0.2 MPa. The difference of estimated adiabatic core temperature caused by the variation of pressure is within 12 K at start of injection. The individual cylinder pressure traces and AHRR profiles for the 16 fired cycles under pilot-fuel injection condition (1) with t_{SE} = 500 microseconds, P_{inj} = 80 MPa and premixed natural gas equivalence ratio ϕ_{NG} = 0.3 for low-load (average IMEP = 0.23 MPa, P_{IN} = 0.1 MPa) and mid-load (average IMEP = 0.7 MPa, P_{IN} = 0.2 MPa) conditions are shown in Fig. 7(a) and Fig. 7(b) respectively.

From Fig. 7, it is clear that the cycle-to-cycle variation is more pronounced at low-load conditions with three individual cycles highlighted by red dashed lines, exhibiting excessive ignition delay resulting in reduced cylinder pressure rise and weak AHRR. As discussed earlier, this strong cycle-to-cycle fluctuation observed at low-load conditions is most likely due to the sharply deteriorating ignition characteristics (increased LTI and HTI delays, less robust transition to HTI) of the pilot-fuel injection in the presence of premixed natural gas.

The change in the ensemble-averaged HTI delay (based on the eight individual pilot-fuel jets from the 16 fired cycles) with natural gas concentration (ϕ_{NG}) for the pilot-fuel injection condition of t_{SE} = 500 microseconds, P_{inj} = 40 MPa under low-load and mid-load intake pressures are shown in Fig. 8(a) and Fig. 8(b) respectively. The HTI delay is defined as the time between the start of injector solenoid energization (13 CAD before TDC) and the start of HTI, which is estimated based on cool-flame chemiluminescence imaging using the methodology described earlier in section 4.1.

It is evident from Fig. 8, that the increase in HTI delay with increasing natural gas concentration is more pronounced at low-load conditions (P_{IN} = 0.1 MPa, Fig. 8(a)) when compared to the corresponding marginal increase in HTI delay observed under mid-load conditions (P_{IN} = 0.2 MPa, Fig. 8(b)).

Under mid-load conditions (P_{IN} = 0.2 MPa) due to the increased thermal mass available for entrainment, the evaporative cooling phase of the pilot-fuel is shortened by about 50%. This rapid-vaporization of the pilot-fuel results in a shorter first-stage, LTI delay followed by a quicker transition into second-stage, HTI without any significant dwell time between the two-stages. The inhibitive effects of natural gas on pilot-fuel ignition characteristics remain, though it appears to be less pronounced at P_{IN} = 0.2 MPa. From, a chemical standpoint, Cantera simulations conducted at higher reactor initial pressures conditions (corresponding to 0.2 MPa intake pressure as shown in Fig. 2(b)) also reveal similar pilot-fuel ignition characteristics namely, shorter LTI delay, near zero dwell transitioning into HTI and less pronounced ignition inhibition effects of natural gas, which is good agreement with the observed experimental results. This is most likely due to an exponential increase in the reactivity rates of reactions that facilitate breakdown of KHP formed during LTI that causes

further rapid decomposition of n-heptane at higher pressures as shown in Fig 9. This ultimately results in faster chain chain-branching reactions after LTI that reduce the dwell time and cause rapid transition into HTI despite the presence of natural gas.

Figures 10(a) and 10(b) show the corresponding fluctuation in the calculated HTI delay values quantified in terms of the coefficient of variation (COV) for the data presented in Fig. 8(a) and 8(b) respectively. The COV of HTI delay exhibits a similar behavior i.e., a near-linear increase with natural gas concentration under low-load conditions (Fig. 10(a)) while remaining almost constant, independent of ϕ_{NG} at mid-load conditions. Thus, it is rather justifiable to attribute the drastic cycle-to-cycle variation observed in Fig. 7 to be at least in part due to a direct consequence of the corresponding fluctuation observed in the HTI delay values. As the primary objective of this work is to gain fundamental insight into the underlying physical and chemical processes that lead to unstable ignition characteristics of the pilot-fuel jet in the presence of natural gas under low-load conditions, we will limit our discussion to low-load intake pressure (P_{IN} = 0.1 MPa) results.

Another aim of this study is to understand the potential effect of LTI on the subsequent HTI. In this study, the 'LTI delay' is defined as the time between the start of solenoid energization and the start of LTI, which is estimated based on cool-flame chemiluminescence imaging using the methodology described earlier in section 4.1. The ensemble-averaged LTI delay and its corresponding COV under low-load conditions (P_{IN} = 0.1 MPa) for the data presented in Figs. 8(a) and 10(a) are shown in Figs. 11(a) and 11(b) respectively. Figure 10 clearly shows that the COV of the LTI delay is rather constant with minimal increase observed beyond ϕ_{NG} = 0.4. However, the LTI delay itself exhibits a direct correlation with increasing natural gas concentrations.

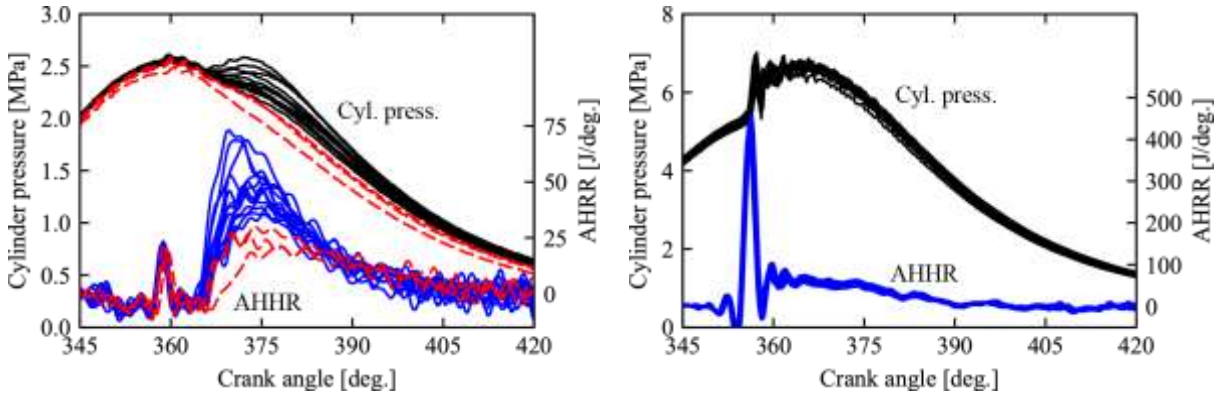

(a) Low-load: P_{IN} = 0.1 MPa (IMEP = 0.23 MPa)

(b) Mid-load: P_{IN} = 0.2 MPa (IMEP = 0.7 MPa)

Figure 7. Individual cylinder pressure (black) traces and AHRR (blue) profiles for the 16 fired cycles for pilot-fuel injection condition (1): t_{SE} = 500 microseconds, P_{inj} = 80 MPa and a premixed natural gas equivalence ratio ϕ_{NG} = 0.3. Weak combustion cycles (partial burns) are highlighted by red dashed lines.

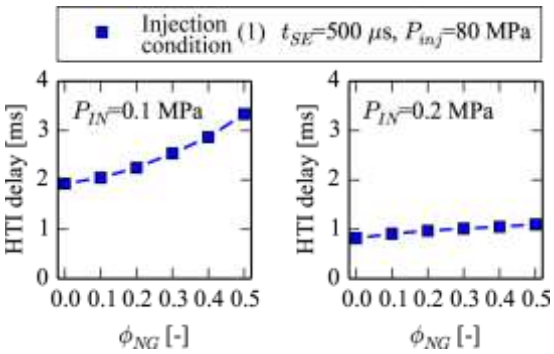

(a) Low-load: P_{IN} = 0.1 MPa (IMEP = 0.23 MPa)

(b) Mid-load: P_{IN} = 0.2 MPa (IMEP = 0.7 MPa)

Figure 8. Ensemble-averaged second-stage, HTI delay for various premixed natural gas concentrations (ϕ_{NG}). Pilot-fuel injection condition (1): t_{SE} = 500 microseconds, P_{inj} = 80 MPa.

1

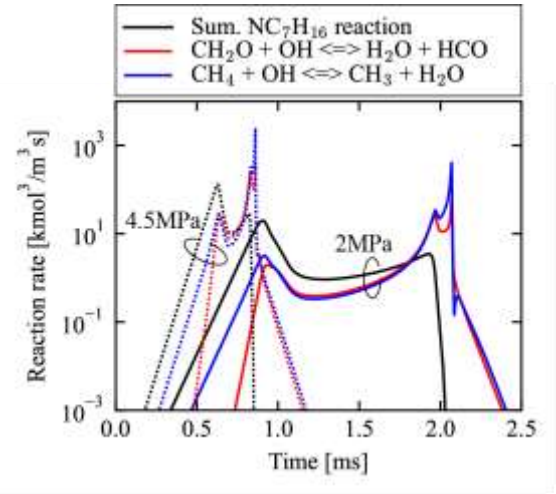

Figure 9. Comparison of reaction rates for 2 MPa and 4.5 MPa.

2

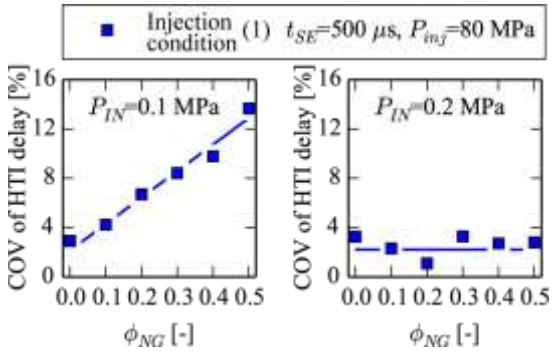

(a) Low-load: P_{IN} = 0.1 MPa (IMEP = 0.23 MPa)

(b) Mid-load: P_{IN} = 0.2 MPa (IMEP = 0.7 MPa)

Figure 10. COV of second-stage, HTI delay for various premixed natural gas concentrations (ϕ_{NG}). Pilot-fuel injection condition (1): t_{SE} = 500 microseconds, P_{inj} = 80 MPa.

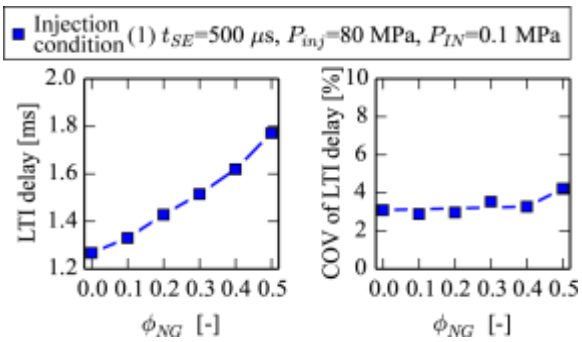

(a) LTI delay (b) COV of LTI delay

Figure 11. Ensemble-averaged first-stage, LTI delay (left) and the corresponding COV (right) for various premixed natural gas concentrations (ϕ_{NG}). Pilot-fuel injection condition (1): t_{SE} = 500 microseconds, P_{inj} = 80 MPa.

4.3 Minimizing spatial and temporal variation of HTI by tailoring pilot-fuel injection parameters

To further understand the physical and chemical processes governing the ignition of pilot-fuel injections into premixed natural gas, and to investigate the cause of unstable ignition under low-load conditions (P_{IN} = 0.1 MPa), the cycle-to-cycle spatial variation in the start of HTI and its correlation to pilot-fuel injection conditions is explored by comparing the cool-flame chemiluminescence snapshots of the eight individual pilot-fuel sprays near the start of HTI for the 16 fired cycles under ϕ_{NG} = 0, 0.3, and 0.5. These snapshots presented in Fig. 12 are cool-flame chemiluminescence images, where the saturation observed after the end of LTI in the form of bright spots indicate ignition kernels that subsequently would initiate HTI.

To contrast the observed spatial and temporal variation in HTI with the near identical (as indicated by the COV of LTI delay) spatial and temporal evolution of LTI, a single representative series of snapshots of cool-flame chemiluminescence taken at fixed crank angle timings (indicated by the labels below) during the LTI phase for ϕ_{NG} = 0, 0.3 and 0.5 is presented in the top panel of Fig. 12 for each of the pilot-fuel injection conditions. Since the fluctuations observed in LTI are small in terms of the start timing, the location of the ignition site, its subsequent spatio-temporal progression, the chemiluminescence intensity and the associated heat release, any series of selected snapshots of cool-flame chemiluminescence from one of the 16 fired cycles can be considered as a representative of that specific dataset. The snapshots of LTI exhibit near identical spatial features with comparable chemiluminescence intensity for all eight sprays irrespective of the pilot-fuel injection condition and the natural-gas concentration. This indicates that the presence of natural gas merely causes a temporal shift in LTI as its spatial evolution remains almost unaffected.

However, the start of HTI is far less stable as indicated by the stark differences in the spatial distribution of the ignition kernels for the 16 fired cycles, irrespective of the pilot-fuel injection parameters. To emphasize this variation, 16 series of HTI snapshots are shown in Fig. 12, ordered by decreasing chemiluminescence intensity, for each of the three pilot-fuel injection conditions under natural gas concentrations of ϕ_{NG} = 0, 0.3 and 0.5.

By comparing the end of injection (based on IR imaging) with the estimated start of LTI from the cool-flame chemiluminescence images, it can be stated that the first-stage LTI begins only after

the end of injection for all the pilot-fuel injection durations utilized in this study. The end of injection event is followed by a transient period of increased entrainment (entrainment wave) which increases mixing rates by up to a factor of three [37, 38]. This results in faster progressive leaning-out of the mixture in the wake region of the pilot-fuel jet, creating fuel-lean regions near the injector. Hence, LTI tends to initiate close to the wake region and proceeds upstream toward the injector as low-temperature autoignition reactions are favored by hotter gases at lean conditions [39-41]. This is immediately followed by the appearance of multiple local hot-spots (indicated by regions of saturation) distributed near the cylinder wall which indicate transition to HTI in the absence of natural gas. In the presence of natural gas, due to its chemical inhibition effect, the LTI tends to initiate much further downstream of the injector, with a prolonged dwell period followed by the appearance of relatively fewer local hot-spots near the cylinder wall, signifying the start of HTI. More detailed discussion detailing the spatio-temporal progression of two-stage autoignition and combustion stability can be found in references [21] and [32] in the manuscript.

As discussed in Section 2.5, the three pilot-fuel injection conditions identified by their $\boldsymbol{P_{inj}}$ and $\boldsymbol{t_{SE}}$ (1): 80 MPa and 500 microseconds, (2): 80 MPa and 760 microseconds and (3): 40 MPa and 760 microseconds will be compared on the basis of identical injection pressure: (1) and (2), identical injection duration: (2) and (3), and equal pilot fuel mass: (1) and (3).

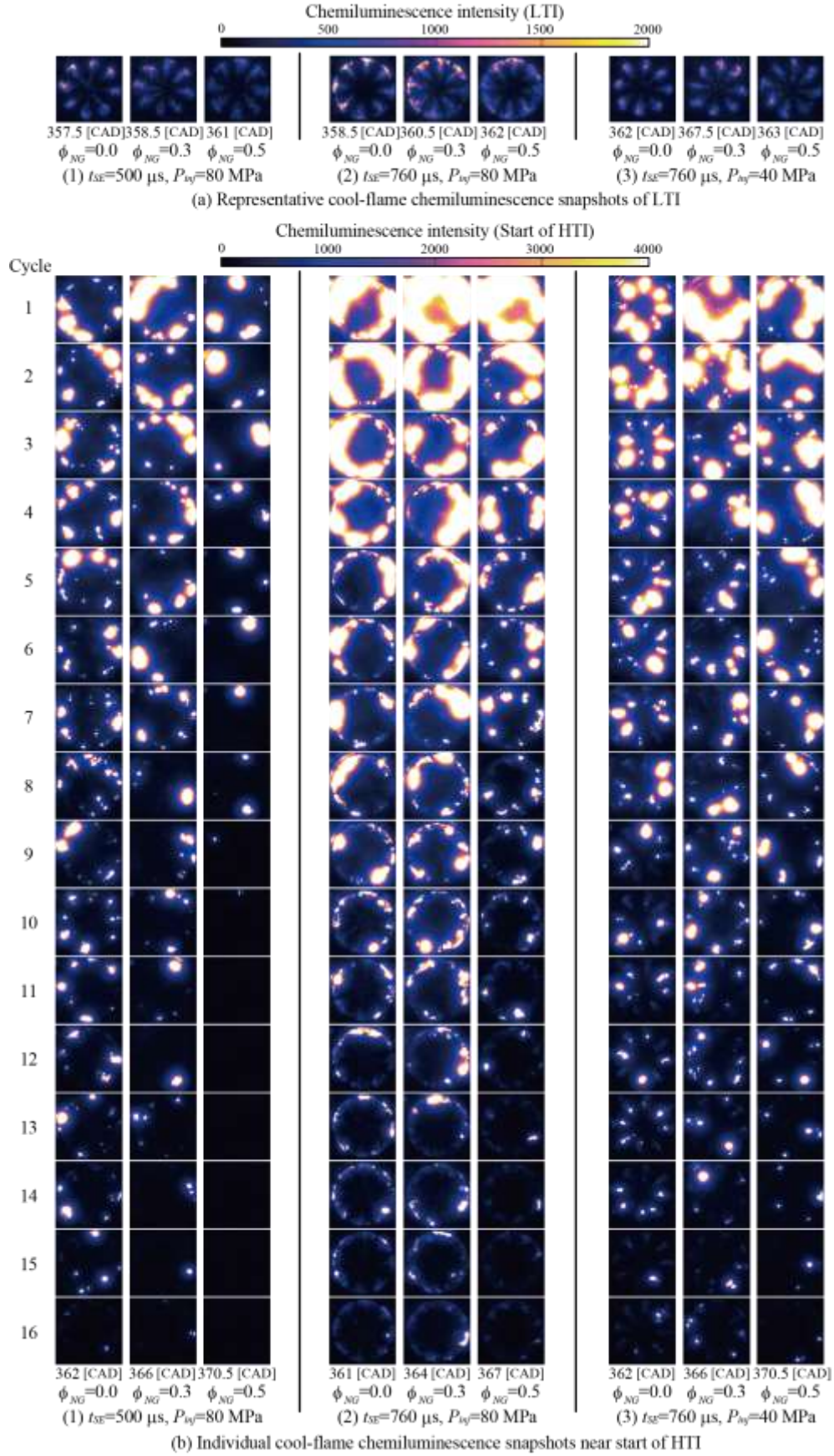

Figure 12. Top: Representative cool-flame chemiluminescence snapshots captured during LTI. Bottom: Individual cool-flame chemiluminescence snapshots taken near the start of HTI from 16 fired cycles. Low-load condition $\boldsymbol{P_{IN}}$ = 0.1 MPa. The individual cycles under each dataset are arranged in the order of decreasing chemiluminescence intensity.

4.3.1 Pilot-fuel injection condition (1): 80 MPa and 500 microseconds

Based on the images presented on the left panel of Fig. 12, grouped under injection condition (1): t_{SE} = 500 microseconds, P_{inj} = 80 MPa, it is clear that the transition to HTI (indicated by the bright spots) occurs in all 16 cycles for ϕ_{NG} = 0 (first column), though the chemiluminescence intensity among the eight pilot-fuel jets is non-uniform, unlike that of LTI.

In the presence of natural gas, the start of HTI becomes unstable in terms of its timing, location and the number of ignition sites for both ϕ_{NG} = 0.3 (second column) and ϕ_{NG} = 0.5 (third column). This is reflected in the random distribution and appearance of ignition sites especially for ϕ_{NG} = 0.5 when compared to ϕ_{NG} = 0. The HTI sites (bright spots) are not present in all of the eight pilot-fuel jets, which indicate the absence of transition to HTI in some of these jets. Among the 16 fired cycles for ϕ_{NG} = 0.5, the last row of images indicate that this cycle exhibits the least chemiluminescence intensity. This signifies failure to transition into HTI, leading to possible misfire or partial burn, which is also in good agreement with the cylinder pressure data. As described earlier in Section 3, the chemical-kinetic simulations indicate that the presence of OH radicals facilitate the transition from LTI to HTI. So it is likely that in the presence of natural gas, the oxidization of CH_4 consumes OH radicals that were produced by n-heptane decomposition during LTI, which might lead to increased HTI delay or complete inhibition of HTI i.e., LTI does not transition into HTI.

4.3.2 Pilot-fuel injection condition (2): 80 MPa and 760 microseconds

The images presented on the center panel of Fig. 12 correspond to injection condition (2): t_{SE} = 760 microseconds, P_{inj} = 80 MPa, which is identical to injection condition (1) in terms of fuel-rail pressure but with a slightly longer injection duration. This increased injection duration injects more than twice the mass of n-heptane compared to injection condition (1), as described in Table 2.

Comparing the two sets of images under injection conditions (1) and (2) for ϕ_{NG} = 0.5 (third column), it is clear that that all eight-fuel jets show strong evidence of transition to HTI in all 16 fired cycles, including least bright cycle (last row) under injection condition (2). For longer pilot-fuel injection durations, the HTI typically appears to initiate at the edge of the piston bowl. Longer injection durations can cause the pilot-fuel jet to penetrate deeper into the piston bowl leading to higher n-heptane fuel concentrations in the outer regions of the piston bowl. This results in the distribution of HTI sites closer to the bowl wall. Furthermore, the higher local concentrations of n-heptane at the ignition sites due to the increased injected fuel mass may partially offset the increased scavenging of OH radicals caused by CH_4 oxidation in the presence of natural gas. Additionally, for longer injection durations, the onset of the entrainment wave [37] after the end of injection that results in increased mixing is delayed, which will allow for richer pilot-fuel mixtures to exist for a longer duration in the jet. Though the delayed onset of the entrainment wave causes reduced mixing that might adversely affect LTI delay, the increased availability of richer pilot-fuel mixtures promote easy transition from LTI to HTI as reported in [21, 32].

Thus, from a practical perspective, for a given pre-pilot, premixed operating equivalence ratio of natural gas and air, it is possible to improve the ignition stability by modifying the pilot-fuel injection parameters. Injection conditions (1) and (2) have a relatively high injection pressure, which increases the entrainment of surrounding natural gas and air mixtures into the pilot-fuel spray when

compared to a lower injection pressure condition such as (3). This causes a rapid decrease in the ratio of pilot-fuel to CH_4 entrained into the jet at higher injection pressures. This decreases the probability of LTI transitioning into HTI due to the ignition inhibition effect of CH_4 oxidization, which consumes OH radicals that play an important role in this transition. By increasing the injected pilot-fuel mass using a longer injection duration, richer pilot-fuel mixtures are made available for a longer time as the increase in mixing due to the entrainment wave that occurs at the end of injection is delayed. Thus the ratio of pilot-fuel to CH_4 entrained into the jet can remain at a higher value for a longer duration thereby promoting the transition from LTI to HTI.

4.3.3 Pilot-fuel injection condition (3): 40 MPa and 760 microseconds.

As an alternative to increasing the injected pilot-fuel mass to increase the ratio of pilot-fuel to CH_4 entrained into the jet, the injection pressure can also be reduced to decrease the rate of entrainment of the ambient mixture into the jet. Keeping in mind the primary intent of natural-gas engines is to reduce exhaust emissions by maximizing the proportion of fuel-lean premixed natural-gas combustion, an approach that does not increase the injected pilot-fuel mass is certainly desirable. To explore the lower injection pressure approach, injection condition (3) with t_{SE} = 760 microseconds, P_{inj} = 40 MPa is chosen. Here the injection pressure is reduced to 40 MPa while the longer injection duration of injection condition (2) is maintained to inject the same mass of pilot-fuel as injection condition (1).

Comparing the two sets of images under injection conditions (1) and (3) for ϕ_{NG} = 0.5 (third column), it is clear that there are more ignition kernels at the start of HTI in all 16 fired cycles with no misfires or partial burns for injection condition (3). Thus, despite injection conditions (1) and (3) injecting the same mass of pilot-fuel, the transition to HTI is more robust under injection condition (3). The potential reasons behind the improved pilot-fuel ignition characteristics observed, despite the presence of natural gas can be explained as follows.

First, the longer injection duration delays the onset of the end of injection entrainment wave, which slows the mixing rate, thereby allowing richer pilot-fuel mixtures to exist for a longer duration in the jet. The increased availability of richer pilot-fuel mixtures promotes robust transition to HTI. Second, comparing the spatial location of LTI initiation based on the top row of images presented in Fig. 12, it can be seen that the LTI for injection condition (3) initiates closer to the center of the combustion chamber than for injection condition (2). As it transitions from LTI to HTI, the ignition kernels at the start of HTI for injection condition (3) are also located closer to the center of the combustion chamber than for injection condition (2). This difference is likely due to the slower penetration rate of the pilot-fuel jet for injection condition (3) caused by the reduced injection pressure despite them both having identical injection duration. Comparing injection condition (3) with (1), the lower injection pressure for injection condition (3) leads to slower entrainment of the premixed natural gas and air into the jet, though both inject the same mass of pilot-fuel. Hence, the combination of slower pilot-fuel jet penetration combined with slower entrainment due to the lower injection pressure slows the rate at which the ratio of pilot-fuel to CH_4 entrained into the jet decreases, thereby decreasing the ignition inhibition effect by minimizing OH consumption due to CH_4 oxidization. Moreover, the longer injection duration further compounds this reduced inhibition effect as the delayed onset of the

entrainment wave reduces mixing thereby resulting in increased and sustained availability of richer pilot-fuel mixtures capable of promoting more effective transition to HTI even in the presence of natural gas.

Figure 13 shows the relationship between HTI delay and its fluctuation represented in terms of its COV for all experiments thereby quantitatively summarizing the changes in ignition for injection conditions (1), (2), and (3) as the premixed natural gas concentration is varied from ϕ_{NG} = 0 to 0.5. The observed increase in the COV of HTI delay with increasing ϕ_{NG} under injection condition (1) can be reduced by either increasing the injection duration leading to increased pilot-fuel mass while maintaining the same injection pressure (injection condition (2)) or by decreasing the injection pressure while maintaining the same pilot-fuel mass using a longer injection duration (injection condition (3)).

Again from Fig. 12, it is clear that the LTI timing for injection condition (3) is later than for injection condition (1) i.e., for example with ϕ_{NG} = 0.5, LTI occurs later at 363 CAD and 361 CAD for injection conditions (3) and (1) respectively. However, the HTI timings for both injection conditions are nearly identical as seen in Fig. 12. The more robust transition from LTI to HTI under injection condition (3) is also apparent from Fig. 14, in which the dwell time between LTI and HTI are presented. The dwell times are clearly shorter for injection condition (3) compared to injection condition (1).

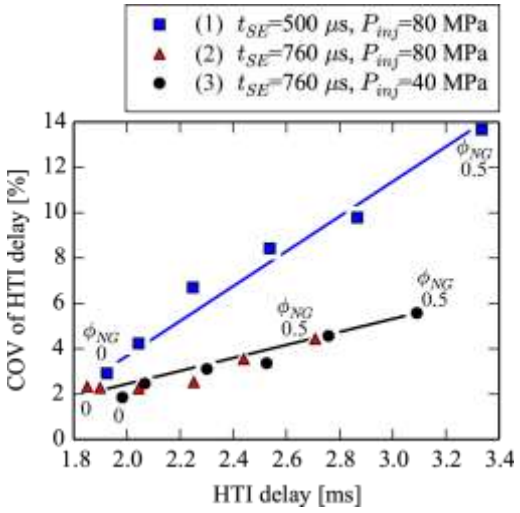

Figure 13. Relationship between HTI delay and its fluctuation represented in terms of its COV.

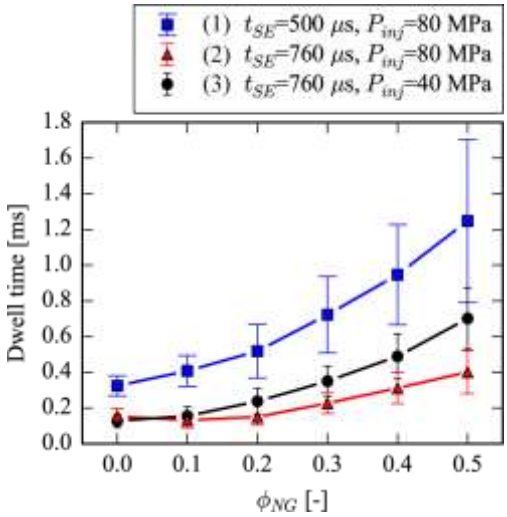

Figure 14. Dwell time between the end of LTI and the start of HTI.

5. Conclusions

The main objective of this study is to visually examine the ignition process in dual-fuel, diesel piloted natural gas combustion inside a heavy-duty optical engine using chemiluminescence imaging diagnostics. This was to facilitate understanding of the physical and chemical processes that govern the ignition stability of the pilot-fuel sprays in the presence of premixed natural gas, so that potential solutions to the issue of unstable ignition under low-load conditions in dual-fuel engines can be formulated. A combination of chemical-kinetics simulations using Cantera in a simplified engine environment and analysis of experimental engine performance and imaging data support the following conclusions.

1) The chemical-kinetics simulations reveal that ignition of the n-heptane pilot-fuel jet in dual-fuel combustion occurs in two stages, and the amount of CH_4 in the ambient mixture affects the timing of those stages. A first-stage, cool-flame, low-temperature ignition (LTI) is followed by a second-stage, high-temperature ignition (HTI). As the concentration of CH_4 entrained into the jet increases, both the onset of LTI and HTI in the pilot-fuel jet are delayed, at least in part due to the scavenging effect of CH_4 on OH radicals that play a critical role in the transition from LTI to HTI.
2) The chemiluminescence imaging diagnostics allowed to track the temporal and spatial progression of LTI and HTI using cool-flame and OH* chemiluminescence emission imaging respectively. The start and end of LTI, start of HTI and the associated dwell time were detected based on the intensity of the cool-flame chemiluminescence images using a comprehensive image analysis methodology.
3) The chemiluminescence imaging diagnostics also allowed for characterizing the cycle-to-cycle and spatial variation in LTI and HTI of the n-heptane pilot-fuel jet for various injection conditions. This was carried out based on analysis of imaging data from the eight individual pilot-fuel sprays for 16 fired cycles.
4) A prominent increase in LTI and HTI delay with increasing natural gas concentrations was observed under low-load conditions ($\boldsymbol{P_{IN}}$ = 0.1 MPa). The increase in ignition delay was more

pronounced for HTI than for LTI. In the case of injection condition (1): t_{SE} = 500 microseconds and P_{inj} = 80 MPa, when ϕ_{NG} was increased from 0.0 to 0.5, the HTI delay increased by 1.4 microseconds, which is approximately twice the corresponding increase in LTI delay.

5) The increase in dwell time between the end of LTI and the start of HTI had a pronounced effect on the observed increase in HTI delay. In the case of injection condition (1): t_{SE} = 500 microseconds and P_{inj} = 80 MPa, when ϕ_{NG} was increased from 0.0 to 0.5, the dwell time increased by 0.9 microseconds, which accounts for around two-thirds of the increase in HTI delay.

6) The increase in both LTI and HTI delay also resulted in a corresponding increase in their respective COV (fluctuations). While the COV of HTI delay was found to linearly increase with increasing HTI delay, the COV of LTI delay remained fairly constant throughout.

7) The apparent increase in the dwell time with natural gas concentration observed for all injection conditions under low-load i.e., P_{IN} = 0.1 MPa is consistent with the simulation results from the simple homogeneous reactor model.

8) The ignition stability deterioration (quantified by the increase in COV of ignition delay) under low-load conditions (P_{IN} = 0.1 MPa) resulted in unstable combustion with possible misfires or partial burns for injection condition (1): t_{SE} = 500 microseconds, P_{inj} = 80 MPa. The ignition stability of the pilot-fuel jet was drastically improved (COV of HTI delay decreased by half) by either increasing the injection duration while maintaining injection pressure that lead to increased pilot-fuel mass (injection condition (2): t_{SE} = 760 microseconds, P_{inj} = 80 MPa) or by decreasing the injection pressure while maintaining constant pilot-fuel mass by using a longer injection duration (injection condition (3): t_{SE} = 760 microseconds and P_{inj} = 40 MPa).

9) The improved ignition characteristics of the pilot-fuel jet in the presence of natural gas under injection condition (3) is likely attributed to a combination of slower pilot-fuel jet penetration combined with slower entrainment due to the lower injection pressure. This slows the rate at which the ratio of pilot-fuel to CH_4 entrained into the jet decreases, thereby decreasing the ignition inhibition effect by minimizing OH consumption due to CH_4 oxidization. The longer injection duration further compounds this reduced inhibition effect as the delayed onset of the entrainment wave reduces mixing thereby resulting in increased and sustained availability of richer pilot-fuel mixtures capable of promoting more effective transition to HTI even in the presence of natural gas.

As the concentration of natural gas in the ambient mixture increases, there is marked deterioration observed in the ignition characteristics of pilot-fuel jet especially at low-load conditions. This can cause subsequent deterioration in combustion stability leading to possible misfires or partial burns resulting in excessive methane slip. Though natural gas concentration can be decreased to improve pilot-fuel ignition characteristics, poor flame propagation due to decreased flame speeds may lead to excessive flame quenching that can exacerbate methane slip. However, the experimental data clearly suggests that for a fixed premixed natural gas fuel-air equivalence-ratio, it is possible to improve the “stability” of the combustion process by solely manipulating the pilot-fuel injection parameters while maintaining constant mass of injected pilot-fuel. This allows for tailoring mixing

trajectories to offset changes in fuel ignition chemistry, so as to promote a robust transition from LTI to HTI by changing the balance between the local concentration of the pilot-fuel and richness of the premixed natural gas and air. This could prove to be a valuable tool for combustion design to improve fuel efficiency or reduce noise or perhaps even reduce heat-transfer losses by locating early combustion away from in-cylinder walls.

6. Acknowledgements

This research was sponsored in part by the U.S. Department of Energy (DOE) Office of Energy Efficiency and Renewable Energy (EERE). Optical engine experiments were conducted at the Combustion Research Facility of Sandia National Laboratories in Livermore, CA. Sandia National Laboratories is a multi-mission laboratory managed and operated by National Technology and Engineering Solutions of Sandia, LLC., a wholly owned subsidiary of Honeywell International, Inc., for the U.S. Department of Energy's National Nuclear Security Administration (NNSA) under contract DE-NA0003525.

References

1) MARPOL ANNEX VI AND NTC 2008 with Guidelines for Implementation 2013 edition. London: International Maritime Organization, 2013.

2) International Maritime Organization. Initial IMO Strategy on Reduction of GHG Emissions from Ships, Resolution MEPC.304(72), London, UK, 2018.

3) Alvarez CEC, Couto GE, Roso VR, Thiriet AB, Valle RM. A review of prechamber ignition system as lean combustion technology for SI engines. Appl Therm Eng 2018; 128:107-120.

4) Karim GA. Dual-Fuel Diesel Engines. CRC Press, 2015.

5) Sommer DE, Yeremi M, Son J, Corbin JC, Gagne S, Lobo P, Miller JW and Kirchen P. Characterization and Reduction of In-Use CH4 Emissions from a Dual Fuel Marine Engine Using Wavelength Modulation Spectroscopy. Environ. Sci Technol 2019; 53:2892-2899.

6) Ushakov S, Stenersen D and Einang PM. Methane Slip Summarized: Lab vs. Field Data. Proceedings of 29th CIMAC Congress, Paper No.63, Vancouver, Canada, 10-14 June 2019.

7) Weisser G, Schneiter D and Nylund I. Greenhous Gas (GHG) Emissions from LNG Engines. Review of the Two-Stroke Engine Emission Footprint. Proceedings of 29th CIMAC Congress, Paper No.426, Vancouver, Canada 10-14 June 2019.

8) Järvi A. Methane slip reduction in Wärtsilä lean burn gas engines. Proceedings of 26th CIMAC Congress, Paper No.106, Bergen, Norway, 14-17 June 2010.

9) Core Writing Team, R.K. Pachauri and L.A. Meyer. Climate Change 2014 Synthesis Report: Synthesis Report. Contribution of Working Groups I, II and III to the Fifth Assessment Report of the Intergovernmental Panel on Climate Change. IPCC, Geneva, Switzerland 2014.

10) Tajima H. Methane Slip Reduction from Marine Gas Engines by Stratified Oxygen concentration using Gas Permeation Membrane. Proceedings of 28th CIMAC Congress, Paper No.162, Helsinki, Finland, 6-10 June 2016.

11) Aaltonen P, Järvi A, Vaahtera P and Widell K. New DF Engine Portfolio (Wärtsilä 4-Stroke). Proceedings of 28th CIMAC Congress, Paper No.251, Helsinki, Finland, 6-10 June 2016.

12) Srna A, Rotz B, Herrmann K, Boulouchos K and Bruneaux G. Experimental investigation of pilot-fuel combustion in dual-fuel engines, Part 1: Thermodynamic analysis of combustion phenomena. Fuel 2019; 255, 115642.

13) Srna A, Rotz B, Bolla M, Wright YM, Herrmann K, Boulouchos K and Bruneaux G. Experimental investigation of pilot-fuel combustion in dual-fuel engines, Part 2: Understanding the underlying mechanisms by means of optical diagnostics. Fuel 2019; 255, 115766.

14) Schlatter S, Schneider B, Wright YM and Boulouchos K. N-heptane micro pilot assisted methane combustion in a Rapid Compression Expansion Machine. Fuel 2016; 179, 339-352.

15) Schlatter S, Schneider B, Wright Y and Boulouchos K. Experimental Study Ignition and combustion Characteristof a Diesel Pilot Spray in a Lean Premixed Methane/Air Charge using a Rapid Compression Expansion Machine. SAE paper 2012-01-0825.

16) Grochowina M, Hertel D, Tartsch S and Sattelmayer T. Ignition of Diesel Pilot Fuel in Dual-Fuel Engines. Journal of Engineering for Gas Turbines and Power 2019; 141, 081021.

17) Grochowina M, Schiffner M, Tartsch S and Sattelmayer T. Influence of Injection Parameters and Operating Conditions on Ignition and Combustion in Dual-Fuel Engines. Journal of Engineering for Gas Turbines and Power 2018; 140, 102809.

18) Rochussen J and Kirchen P. Characterization of reaction zone growth in an optically accessible heavy-duty diesel/methane dual-fuel engine. Int. J. Engine Res. 2019; 20, 483-500.

19) Rochussen J, Yeo J and Kirchen P. Effect of Fueling Control Parameters on Combustion and Emissions Characteristics of Diesel-Ignited Methane Dual-Fuel Combustion. SAE paper 2016-01-0792.

20)Jie L, Yang F, Wang H, Ouyang M and Hao S. Effects of pilot fuel quantity on the emissions characteristics of a CNG/diesel dual fuel engine with optimized pilot injection timing. Applied Energy 2013; 110, 201-206.

21) Rajasegar R, Niki Y, Li Z and Musculus M. Spatio-Temporal Progression of Two-Stage Autoignition for Diese Sprays in a Low-Reactivity Ambient: n-Heptane Pilot-Ignited Premixed Natural Gas. Proceedings of Western States Section Combustion Institute Fall 2019 Technical Meeting, Paper: 9112-0067, Albuquerque, USA, 14-15 Oct. 2019.

22) Reactors and Reactor Networks, Available at: https://cantera.org/science/reactors.html#reactors-and-reactor-networks (accessed 24 June 2020).

23) Goodwin G, Moffat H and Speth R. Cantera: An object-oriented software toolkit for chemical kinetics, thermodynamics, and transport processes, version 2.1.1, 2014.

24) Mehl M, Pitz WJ, Westbrook CK and Curran HJ. Kinetic Modeling of Gasoline Surrogate Components and Mixtures under Engine Conditions. Proceedings of the Combustion Institute 2011; 33, 1, 193-200.

25) Dec JE. A conceptual model of DI diesel combustion based on laser-sheet imaging. SAE paper 970873, 1997.

26) Farrell JT, Cernansky NP, Dryer FL, Law CK, Friend DG, Hergard CA, McDavid RM, Patel AK, Mueller CJ and Pitsch H. Development of an Experimental Database and Kinetic models for Surrogate Diesel Fuels. SAE paper 2007-01-0201.

27) Heywood JB. Internal Combustion Engine Fundamentals. McGraw-Hill, Inc., 1988.

28) Pickett LM, Siebers DL and Idicheria CA. Relationship Between Ignition Processes and the Lift-Off Length of Diesel Fuel Jets. SAE paper 2005-01-3843.

29) Siebers D and Higgins B. Flame Lift-Off on Direct-Injection Diesel Sprays Under Quiescent Conditions. SAE paper 2001-01-0530.

30) Hultqvist A, Christensen M, Johansson B, Franke A, Richter M and Alden M. A Study of the Homogeneous Charge Compression Ignition Combustion Process by Chemiluminescence Imaging. SAE paper 1999-01-3680.

31) Dec JE, Hwang W and Sjöberg M. An Investigation of Thermal Stratification in HCCI Engines

Using Chemiluminescence Imaging. SAE paper 2006-01-1518.

32) Rajasegar R, Niki Y, Li Z, Garcia-Oliver JM and Musculus MPB. Spatio-Temporal Progression of Two-Stage Auto-Ignition of Diesel Sprays in a Low-Reactivity Ambient Fuel-Air Mixture, Proceedings of the Combustion Institute, 2020, doi: https://doi.org/10.1016/j.proci.2020.11.005.

33) Mastorakos E. Ignition of turbulent non-premixed flames. Progress in Energy and Combustion Science 2009; 35, 57-97.

34) Idicheria CA and Pickett LM. Ignition, soot formation, and end-of-combustion transients in diesel combustion under high-EGR conditions. Int. J. Engine Res. 2011; 12, 376-392

35) Musculus MPB, Miles PC and Pickett LM. Conceptual model for partially premixed low-temperature diesel combustion. Progress in Energy and Combustion Science 2013; 39, 246-283.

36) Ando H, Sakai Y and Kuwahara K. Universal Rule of Hydrocarbon Oxidation. SAE paper 2009-01-0948.

37) Musculus MPB and Kattke K. Entrainment Waves in Diesel Jets. SAE paper 2009-01-1355, 2009.

38) Musculus MPB, Lachaux T, Pickett LM and Idicheria CA. End-of-Injection Over-Mixing and Unburned Hydrocarbon Emissions in Low-Temperature-Combustion Diesel Engines. SAE paper 2007-01-0907, 2007.

39) Srna A, Bolla M, Wright YM, Herrmann K, Bombach R, Pandurangi SS, Boulouchos K and Bruneaux G. Effect of methane on pilot-fuel auto-ignition in dual-fuel engines. Proceedings of the Combustion Institute 2019; 37, 4741-4749.

40) Krisman A, Hawkes ER and Chen JH. Two-stage autoignition and edge flames in a high pressure turbulent jet. J. Fluid Mechanics 2017, 824, 5-41.

41) Dahms RN, Paczko GA, Skeen SA and Pickett LM, Understanding the ignition mechanism of high-pressure spray flames. Proceedings of the Combustion Institute 2017; 36, 2615-2623.